



Fabrication of a Carbon Steel-to-Stainless Steel Transition Joint Using Direct Laser Deposition — A Feasibility Study

Results indicated a graded joint with a smooth microstructural transition is possible

BY J. D. FARREN, J. N. DuPONT, AND F. F. NOECKER II

ABSTRACT. Dissimilar metal weld (DMW) failures between carbon steels and stainless steels still occur in many industrial applications. These failures have generally been attributed to the very sharp changes in composition and corresponding microstructure that occur along the weld interface and the formation of locally high stresses associated with thermal expansion mismatch. The formation of a soft carbon denuded region near the weld interface has been identified as a key factor that leads to accelerated creep failure under the combined influences of service and thermally induced stresses. This suggests that such failures could be substantially minimized or eliminated by the development of a transition joint in which the composition is varied in a controlled manner over relatively large distances. With this approach, the transition joint could be inserted between the carbon steel and stainless steel end members to permit the deposition of two similar welds at either end of the joint, replacing the single dissimilar weld that is prone to failure. The feasibility of fabricating such a transition joint for this application using the direct laser deposition process is assessed in this research.

A Laser Engineered Net Shaping (LENS®) unit was used to prepare a transition joint between 1085 carbon steel and 316 stainless steel. Microstructural development of the transition joint was studied using a combination of compositional analysis, hardness testing, light optical microscopy, and scanning electron microscopy. The results showed that a

graded joint can be fabricated with a smooth transition in composition from the 1085 steel to 316 stainless steel over a distance of ~ 2 inches. Other grade lengths can also be prepared. The transition joint consisted of four microstructurally distinct regions. A region that was predominately austenite existed over most of the grade. This region was followed by a dual-phase austenite/martensite region near the interface between the grade and the 1085 steel. The final section consisted of a uniform composition equivalent to the 1085 end member. Most of this region appeared to contain tempered martensite with a uniform hardness. The final layer in this region had high hardness associated with the presence of as-quenched martensite. Except for two localized increases in hardness, the transition exhibited a smooth variation in hardness from one end of the joint to the other. Microstructural evolution within each of the regions was interpreted by combining both nominal and localized composition measurements with the WRC and Schaeffler constitution diagrams. Directions for future research needed to fully optimize this approach are briefly discussed. The results of this work form the basis for more detailed

investigations required to optimize the performance of this approach in actual service conditions.

Introduction

Failure of Dissimilar Metal Welds

Many applications exist in industry that require joining of carbon steels to stainless steels. A typical example can be found in power generation applications. The primary boilers and heat exchangers in coal-fired power plants operate at temperatures and environments that permit the use of inexpensive ferritic alloy steels, while the superheater and reheater areas operate at higher temperatures and under more severe corrosion conditions that require the use of austenitic stainless steels. A dissimilar metal weld (DMW) must be made at the alloy steel-to-stainless steel transition region. These DMWs are often prone to premature failure when exposed to elevated service temperatures. Much work has been done to understand the mechanism of DMW failures in such applications.

In the as-welded condition, a composition gradient develops near the weld interface of the DMW due to partial mixing between the two materials (Refs. 1, 2). The relatively high hardenability associated with this composition gradient, combined with the high cooling rates associated with fusion welding, produce a thin layer of martensite at the weld interface (Ref. 3). It is common to observe hardness differences of more than 200 Vickers over distances as short as 250 μm in this transition region. Most applications require that the weld be postweld heat treated (PWHT) before being used in service in order to reduce residual stresses and temper the martensite re-

KEYWORDS

Dual Phase
Dissimilar Metal Weld
Graded Joint
Laser
LENS®
Stainless Steel
Transition Joint

J. D. FARREN, J. N. DuPONT, and F. F. NOECKER II are with Department of Materials Science and Engineering, Lehigh University, Bethlehem, Pa.

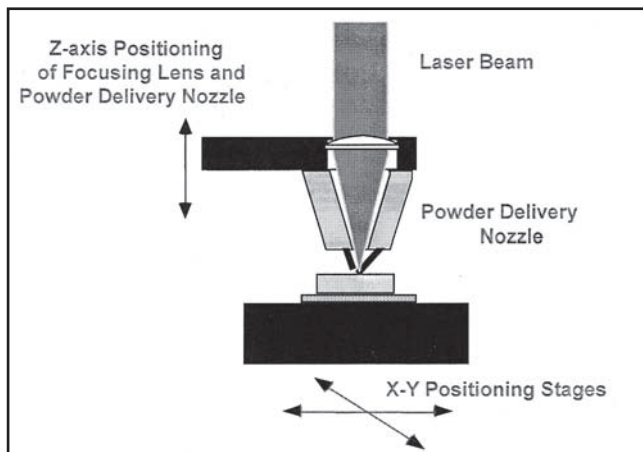


Fig. 1 — Schematic illustration of the LENS® process.

gion, and further microstructural evolution occurs during the PWHT.

Stainless steel alloys typically have lower carbon levels than the alloy steels (e.g., ~ 0.03–0.08 wt-% C in stainless steels compared to ~ 0.10–0.15 wt-% C in alloy steels). This leads to a carbon concentration gradient across the DMW joint. Austenitic stainless steels exhibit a high solubility for carbon and a relatively low diffusivity, while ferritic steels exhibit relatively low solubility and high diffusivity. These differences in carbon solubility and diffusivity, combined with the carbon concentration gradient, strongly promote carbon migration (i.e., from the high-carbon alloy steel side toward the lower-carbon stainless steel side of the joint) (Ref. 3). Localized variations in carbon concentration have been measured to be as high as 0.7 wt-% to below about 0.01 wt-% over distances on the order of 100 μm (Ref. 6).

This severe carbon concentration gradient has several important effects on the microstructure and properties of the DMW. Within the alloy steel side, carbon depletion leads to a significant localized reduction in the creep strength. The increase in carbon content within the transition region affects the microstructure during PWHT in two ways (Ref. 3). First, it lowers the A_{c1} temperature below that of the PWHT temperature, so that austenite exists in the transition region during PWHT. Second, the carbon combines with Cr to form chromium carbides during PWHT. This not only provides an additional localized increase in hardness, but also removes Cr and C from solution, which has the effect of raising the martensite start temperature. Thus, upon cooling from the PWHT, the region that was austenite with carbides during PWHT transforms into a microstructure consisting of carbides in an as-quenched marten-

sitic matrix. The hardness in this region can be as high as ~ 500 Vickers. Several hundred microns from this, the carbon-denuded ferritic zone can exhibit a reduced hardness on the order of ~130 Vickers (Ref. 3). Thus, the original strength gradient that existed in the as-welded condition is exacerbated even further after the PWHT.

Failure of DMWs in service has been attributed to the sharp microstructural gradients described previously combined with significant differences in thermal expansion between the two materials (Refs. 5–8). In fact, the coefficient of thermal expansion (CTE) of austenitic stainless steels are ~ 30% higher than alloy steels over typical operating temperatures of coal-fired power plants. King et al. (Ref. 9) used finite element modeling to show that stresses at the weld interface due to this CTE mismatch can be as high as 34 ksi for a temperature change of only 170°C, a temperature change that is readily achieved in operating conditions of coal-fired power plants. In view of these factors, the failure of DMWs can be summarized as follows. A carbon-depleted region exists on the ferritic side that has significant localized reductions in creep strength. The region directly adjacent to this (typically within 100–300 μm) possesses a martensitic matrix with chromium carbides that exhibits significantly higher strength. As a result, strains induced from external service stresses, which are appreciably amplified from additional stresses due to CTE mismatch, are forced onto the soft, low

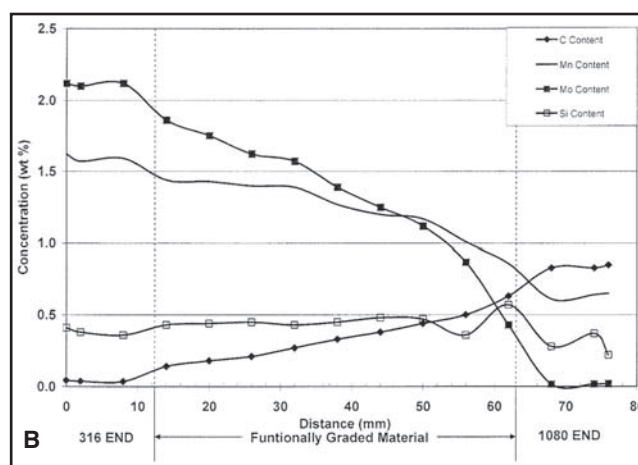
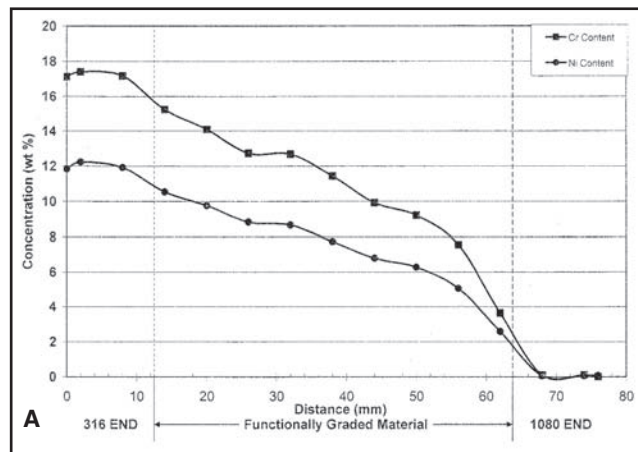


Fig. 2 — Variation in chemical composition along the transition joint for A — Ni and Cr; B — C, Mn, Mo, and Si.

creep strength ferritic side of the joint. This localized strain is relieved by accelerated creep at the service temperature, which results in eventual failure by link up of creep voids within the carbon-denuded zone. This mechanism has been supported by careful characterization of both laboratory and field-induced failures (Refs. 5–8).

Research has been conducted to show that the life of DMWs can be extended by the use of Ni-based filler metals and joint designs with wide included angles (Ref. 10). The Ni-based filler metals have a CTE intermediate to those of the alloy steel and stainless steel, which helps reduce thermal stresses that arise due to CTE mismatch. Joint designs with wide included angles help reduce the axial tensile stress that is oriented perpendicular to the creep-susceptible weld interface, thus minimizing the creep rate of that area. A survey conducted by the Electric Power Research Institute (Ref. 11) has shown that the use of wide included angles and Ni-based filler metals can extend the life of dissimilar metal welds by a factor of approximately six. Although these changes help extend

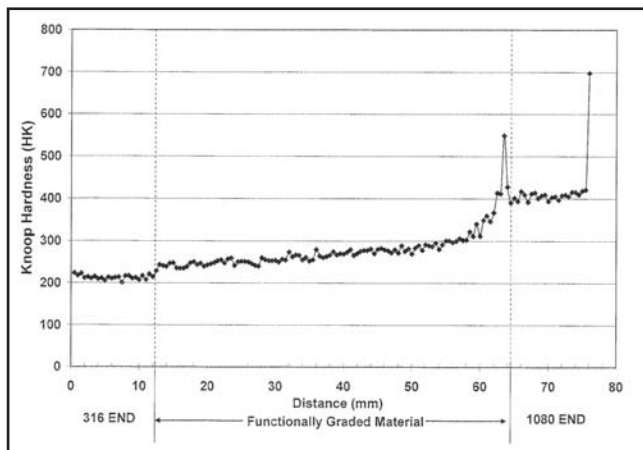


Fig. 3 — Variation in microhardness along the transition joint.

the life of DMWs, they do not provide a long-term solution to the problem because failures still occur in joints prepared with these modifications.

Direct Metal Deposition of Transition Joints

Direct metal deposition (DMD) refers to a variety of solid free-form fabrication processes that are capable of producing fully dense complex shapes directly from a computer-aided design (CAD) drawing. Laser Engineered Net Shaping (LENS®) is a particular DMD process that uses a computer-controlled laser system integrated with dual powder feeders. As shown in Fig. 1, the LENS process utilizes a Nd-YAG laser to produce a melt pool on a substrate attached to an X-Y table. Powder from the dual coaxial powder feeders is injected into the melt pool as the table is moved along a predesigned two-dimensional tool path that is “sliced” from the three-dimensional CAD drawing. A fully dense part is produced by depositing successive line builds, which are built into sequential layers. The dual-powder feeders can be controlled independently so that the composition can be changed at various locations within the part for optimized mechanical and/or corrosion performance. In addition, a melt pool sensor is used to eliminate variations in the pool size that occur due to changes in heat flow associated with variations in part dimensions. The melt pool sensor forms a closed-loop system with the laser power so that the power is automatically varied in real time to maintain a constant pool size.

The relatively high cooling rates associated with laser processing has been shown to produce refined microstructures with improved mechanical properties (Refs. 12, 13). Recent research has also shown this process is well suited for fabrication of functionally graded materials

(Refs. 14–17). Thus, this process appears to be well suited for fabricating carbon steel-to-stainless steel transition joints in which the composition is varied in a controlled manner over relatively large distances. Such a transition joint, in which the sharp changes in composition, microstructure, and concomitant thermal and mechanical properties over short distances are avoided, may help reduce or eliminate the DMW failure problem described above. With this approach, the transition joint could be inserted between a carbon steel to stainless steel transition to permit the deposition of two similar welds at either end of the joint, replacing the single dissimilar weld that is prone to failure. Thus, the objective of this research is to assess the feasibility of fabricating such a transition joint for this application using the LENS process. The results of this work can then form the basis for more detailed investigations required to optimize the performance of this approach in actual service conditions.

Experimental Procedure

An Optomec Model 750 LENS® direct laser deposition unit was used to build a 76.2-mm- (3-in.-) long transition joint tube with an outer radius of 15.9 mm (0.625 in.) and wall thickness of 6.4 mm (0.25 in.). These dimensions were chosen because they represent typical tube dimensions used by the power industry for waterwall panels in fossil-fired boilers.

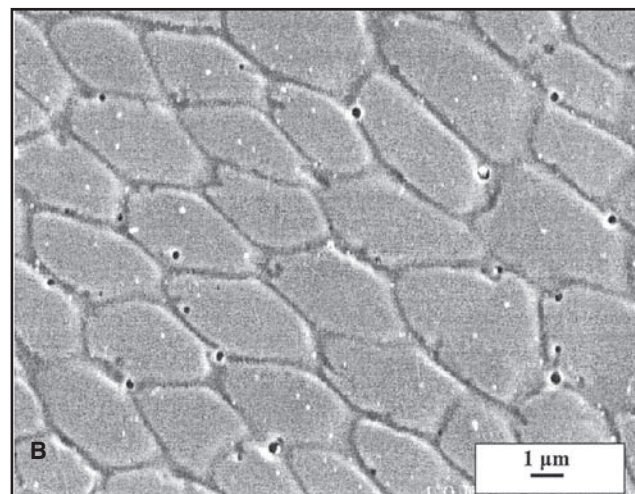
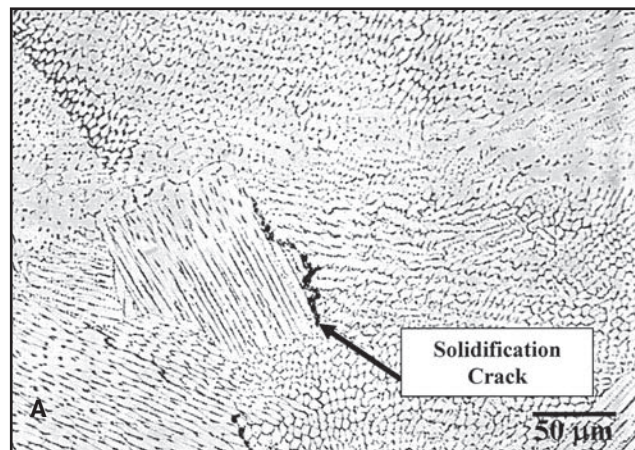


Fig. 4 — Typical microstructure observed at locations from the 316 end to ~ 62 mm from the 316 end of the joint. Etchant — 10% oxalic electrolytic etch, 3 V, 5 s. A — Light optical photomicrograph; B — scanning electron photomicrograph.

The transition joint was fabricated by first depositing 12.7 mm (0.5 in.) of SAE 316 stainless steel onto an AISI 1020 steel substrate. Next, 50.8 mm (2 in.) of functionally graded material was deposited in which the SAE 316 composition changed gradually to AISI 1085 steel, and concluded with 12.7 mm of AISI 1085 steel. In practice, a much lower carbon content alloy steel would be used for this application. The 1085 steel powder was chosen here because, at the time of fabrication, it was the only powder commercially available that had the highly spherical morphology and particle size range required for LENS processing.

The transition joint was fabricated using a travel speed of 16.9 mm/s (40 in./min) and an initial laser power of 350 W. The laser power was then varied automatically on the fly to keep the melt pool shape constant by use of a closed loop melt pool sensor (MPS). The MPS operates by continually measuring the size of the pool with an infrared camera and adjusting the

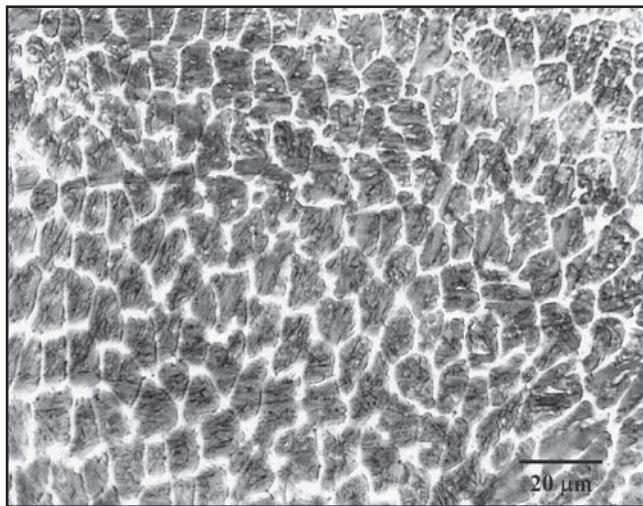


Fig. 5 — Light optical photomicrograph showing the microstructure at ~ 64 mm from the end of the joint where the localized hardness peak was observed. Etchant — 2% nital + sodium metabisulfite.

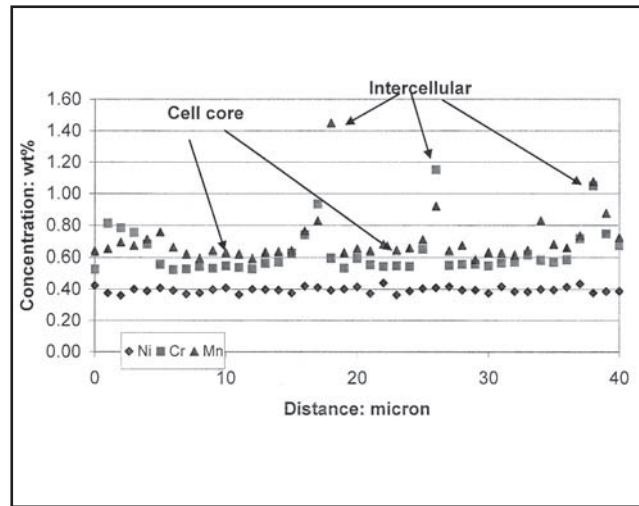


Fig. 6 — EPMA trace showing variation in chemical composition across several of the cells shown in Fig. 5.

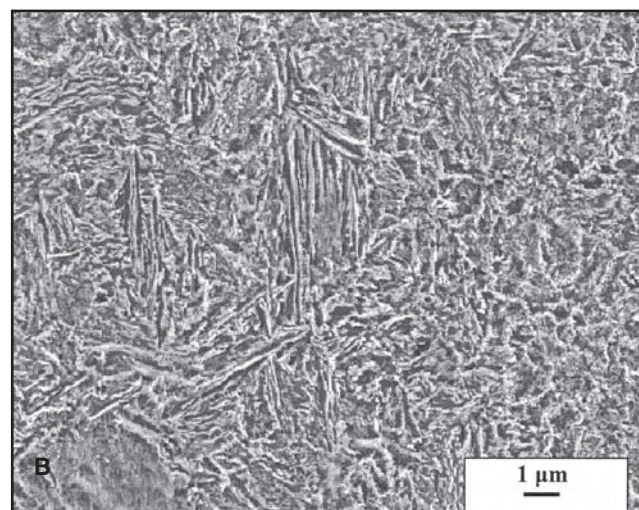
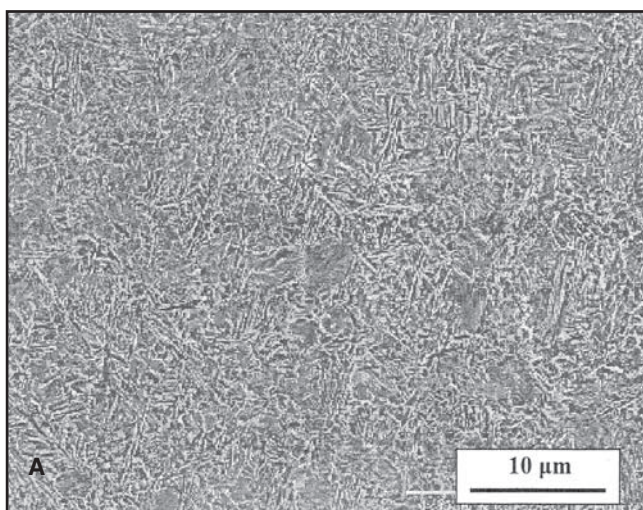


Fig. 7 — SEM photomicrographs of the microstructure observed from ~ 65 mm to the second to last layer of the joint where the hardness is relatively constant. Etchant — 4% picral.

laser power to keep the pool size constant. Each layer in the transition joint was 254 μm (0.01 in.) thick. The initial 12.7 mm length of 316 stainless steel was deposited using 50 layers. The transition region was deposited with 200 layers in which the powder feeders containing each alloy were linearly changed in each layer to vary the composition throughout the graded region. A final 50 layers of 1085 steel was then deposited to complete the transition joint. The entire fabrication required approximately three hours and was conducted in the automatic mode with no need for operator interaction.

Samples were removed from various locations along the transition joint for microstructural analysis. Samples were sectioned and mounted in cold-setting epoxy

and prepared to a 0.05-μm finish using colloidal silica and standard metallographic techniques. A wide variety of etchants was required to observe the range of microstructures, and the best etchant was chosen for each location (listed with each photomicrograph). Microstructural characterization was performed along the length of the sample using both light optical microscopy and scanning electron microscopy. Four-millimeter-thick sections were then prepared for wet chemical analysis at 13 locations along the joint. Local compositional measurements were also acquired using electron probe microanalysis (EPMA) operating at 15-kV accelerating voltage and 65-nA beam current. This accelerating voltage was chosen to minimize the x-ray emission volume

while still exciting K_{α} x rays. Hardness measurements were acquired along the joint using a Knoop indenter and a 1000-g load for 15 s. Five measurements were taken at each location with a 0.5-mm increment between locations, for a total of 760 measurements.

Results

The variation in chemical composition (as determined from wet chemical analysis) along the transition joint is presented in Fig. 2. The first and final 12.7 mm (0.5 in.) ends of the joint have relatively constant compositions. The 50.8 mm (2 in.) length of graded material between the ends varies gradually from 316 stainless steel to 1085 carbon steel. The microhard-

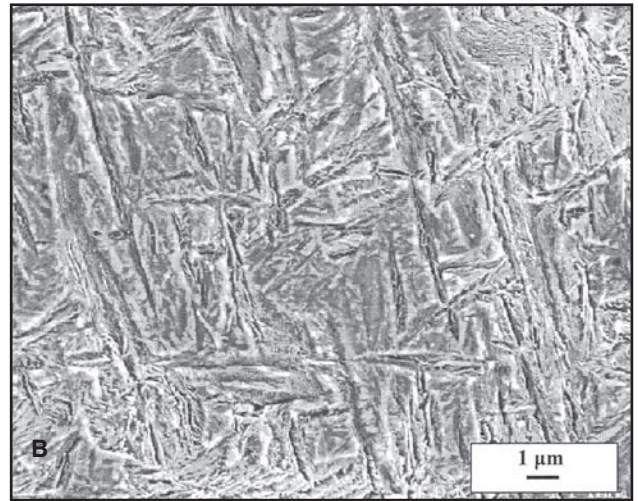
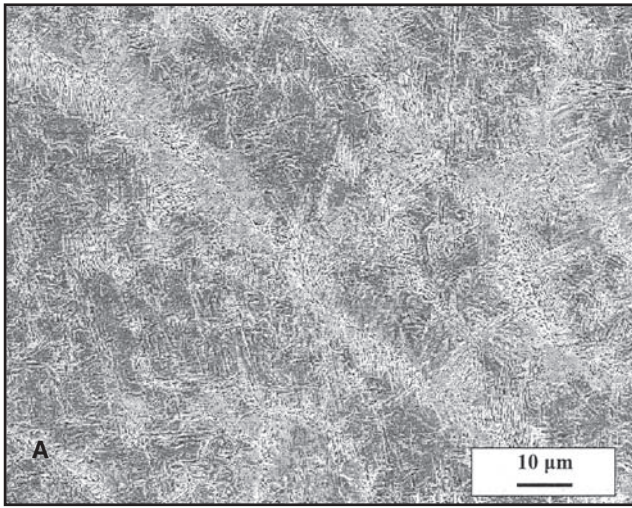


Fig. 8 — SEM photomicrograph showing the microstructure observed in the final layer of the joint that was associated with the highest hardness. Etchant — 4% picral.

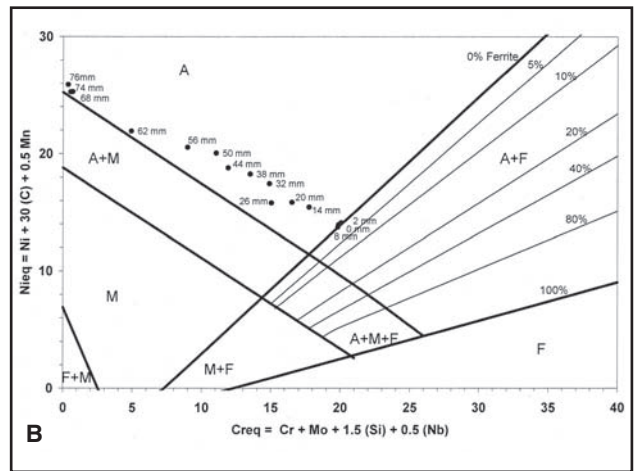
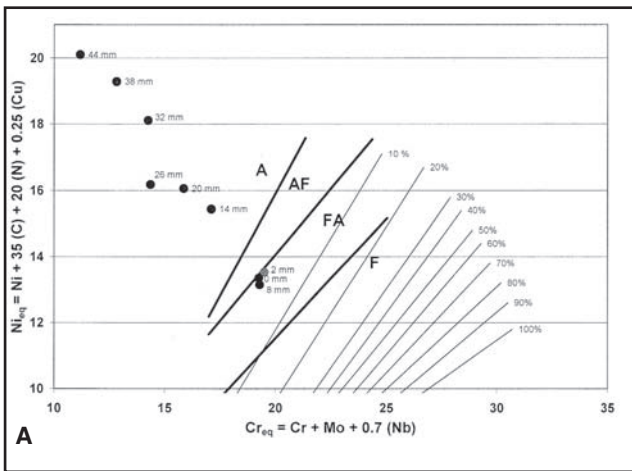


Fig. 9 — Composition measurements from Fig. 1 plotted. A — WRC diagram; B — Schaeffler diagram.

ness results are presented in Fig. 3. The extremities of the 316 and 1085 ends of the transition joint are noted in the figure. The hardness changes in a relatively smooth fashion with two notable exceptions. Local increases in hardness occur at the interface between the functionally graded material and the AISI 1085 end (at ~ 64 mm) and the final layer of the 1085 steel.

Figure 4 shows photomicrographs of the microstructure that was representative of locations from the 316 end to ~ 62 mm from the 316 end of the joint. The microstructure in this region exhibited an austenitic matrix with solidification cells that is typical for a stainless steel in which the primary solidification mode is austenite. There may be small amounts of ferrite within the interdendritic region that formed at the end of solidification due to segregation of Cr and Mo, but the mi-

crostructure within this region is nearly fully austenitic. The austenite cell spacing in this region is ~ 3 μm. The relation between cooling rate (ϵ) and cell spacing (λ) for 310 stainless steel is given by $\lambda = 80\epsilon^{-0.3}$ (Ref. 18), where λ is in μm and ϵ is in $^{\circ}\text{C}/\text{s}$. This relation should provide a good estimate of the cooling rate in this application since the 316 stainless steel used in this work and 310 stainless steel each exhibit an austenitic solidification mode. Based on the measured cell spacing, the cooling rate is estimated to be ~ 5×10^4 $^{\circ}\text{C}/\text{s}$. Cracks were occasionally observed along the interdendritic and grain boundary regions. The location and morphology of these cracks are consistent with solidification cracks and can be attributed to the primary austenitic solidification mode within this region.

Figure 5 shows the microstructure at

~ 64 mm from the end of the joint where the localized hardness peak was observed. This region shows remnant austenite cells similar to that observed in the previous segment of the joint. However, the regions within the cells have transformed to martensite. Retained austenite exists within the cell boundaries. Figure 6 shows an EPMA trace that was acquired across several of the cells shown in Fig. 5. Note that the distribution of Ni is fairly uniform while Cr and Mn have segregated to the intercellular regions. This distribution pattern is typical for a stainless steel alloy that exhibits an austenitic primary solidification mode (Ref. 19). The distribution of Mo could not be measured with the diffracting crystals used in this work, but this element is known to segregate to the interdendritic regions during primary austenite solidification in a manner simi-

lar to Mn and Cr (Ref. 20).

Figure 7 shows SEM photomicrographs of the microstructure that was typical from ~ 65 mm to the second to last layer of the joint where the hardness is relatively constant. The microstructure in this region is very fine (due to the relatively high cooling rates associated with the laser processing) and appears to exhibit a combination of bainite/ferrite and tempered martensite. Figure 8 shows the microstructure observed in the final layer of the joint that was associated with the highest hardness. As with the previous region, the microstructure in this region is extremely fine and difficult to resolve with SEM techniques. As discussed in more detail below, the presence of untempered martensite would be consistent for this composition and high cooling rate, and would account for the hardness peak observed in this final layer.

Discussion

The chemical analysis results shown in Fig. 2 demonstrate the feasibility of the LENS process for fabricating carbon steel to stainless steel transition joints with well-controlled variations in composition. The smooth transition in composition led to a concomitant gradual increase in hardness, except for the two peak hardness locations noted above. Microstructural evolution and the corresponding hardness variations can be understood by plotting the Cr_{eq} and Ni_{eq} values associated with the compositional data from Fig. 2 directly on the WRC and Schaeffler stainless steel constitution diagrams as shown in Fig. 9. The locations along the length of the transition joint associated with each Cr_{eq} and Ni_{eq} value are shown within the plots for reference. The Schaeffler diagram is useful because it contains a martensite line that is pertinent to this work, while the WRC diagram is useful because it aids in identifying the expected primary solidification mode. (Cr_{eq} and Ni_{eq} values plotted on the WRC diagram are limited to locations from 0 to 44 mm along the transition joint due to the more limited composition space associated with the WRC diagram.)

The composition of the 316 powder used here exhibits Cr_{eq} and Ni_{eq} values that place it very close to the boundary separating the AF and FA solidification modes on the WRC diagram. The microstructure observed in this region (Fig. 4) clearly solidified in the A or AF mode. Note that the Schaeffler Cr_{eq} and Ni_{eq} values for the 316 also place it very close to the boundary at which a fully austenitic microstructure would be expected. Thus, the observed primary austenite solidification mode can be attributed to the slight inaccuracies of the diagrams in regions

close to the boundaries or a shift in primary solidification mode induced by the relatively high cooling rate conditions. In either case, the austenitic microstructure observed at the 316 stainless steel end is consistent for the composition and cooling rate conditions in this region.

Successive additions of 1085 steel into the 316 stainless steel within the graded region has the effect of decreasing the Cr_{eq} and increasing the Ni_{eq} . The decreased Cr_{eq} is expected when a stainless steel is diluted with a carbon steel, while the increase in Ni_{eq} can be attributed to the high carbon content of the 1085 powder used in this particular application. (As mentioned previously, the 1085 powder was used here because, at the time of fabrication, it was the only powder commercially available that had the spherical morphology and particle size range required for LENS. Lower carbon alloy steel powders would likely be used in actual practice.) This variation in composition causes the Ni_{eq} and Cr_{eq} values to move from that of the 316 into the fully austenitic phase field in both the WRC and Schaeffler diagrams, and this accounts for the fully austenitic microstructure observed from the 316 end to ~ 62 mm from the 316 end of the joint.

The first hardness spike observed at ~ 64 mm can be attributed to the formation of martensite in this region. The compositional data plotted on the Schaeffler diagram in Fig. 9B show that the Cr_{eq} and Ni_{eq} values are approaching the austenite + martensite phase field of the diagram as the 1085 end of the transition joint is reached. Based on the Cr_{eq} and Ni_{eq} values derived from the nominal composition values plotted in Fig. 9B, and assuming the Schaeffler A + M phase boundary line is highly accurate for this compositional range, martensite would not be expected to form because the Cr_{eq} and Ni_{eq} values never enter into the A + M phase field. This apparent discrepancy can be understood by considering the localized variation in composition that exists across the austenite cells due to microsegregation, as shown previously in Fig. 6. Note that the alloy content is lowest in the cell cores and highest in the cell boundaries. As a result, the Cr_{eq} and Ni_{eq} values are lower in the cell interior regions compared to those in the cell boundaries. This has the effect of shifting the Cr_{eq} and Ni_{eq} values of the cores down and to the left into the A + M phase field, and this accounts for the presence of martensite in the cell core regions. By comparison, the relatively high alloy content in the cell boundaries shifts the Cr_{eq} and Ni_{eq} values up and to the right into the single-phase austenite phase field, which has the effect of stabilizing austenite in the cell boundaries.

This effect can be viewed in a more basic

way by considering the influence of alloying additions on the martensite start temperature (M_s). It is well known that alloying elements such as Mn, Ni, Cr, and Mo reduce the M_s temperature (Ref. 21). Carbon has an even stronger effect on lowering the M_s temperature than the substitutional alloying elements. However, it is well known (Ref. 22) that C diffusion in austenite is high enough to avoid the microsegregation exhibited by the substitutional alloying elements. Thus, the C concentration across the cells is expected to be uniform and would not cause any variation in the M_s temperature across the cells. (Carbon cannot be measured accurately using EPMA techniques.) Microsegregation of the substitutional alloying elements effectively leads to a variation in M_s temperature across the cells. The M_s temperature is above room temperature in the cell core regions, leading to martensite formation. The relatively high alloy content of the cell boundaries lowers the M_s temperature below room temperature, which has the effect of stabilizing the austenite at this location. Finally, the increased hardenability caused by the slightly elevated alloy content in this region (relative to 1085 steel), combined with the high cooling rate associated with laser processing, provides conditions in which the M_s temperature is reached in the core regions before any diffusional-type transformations can occur. These factors account for the microstructure shown in Fig. 5 and localized hardness peak shown in Fig. 3.

The final region of the transition joint consists of laser-deposited "pure" 1085 steel. The layers that experienced post-deposition thermal excursions from subsequent passes exhibited a constant hardness of about 400 Knoop, while the very last pass exhibited a hardness of 700 Knoop. The microstructure in this region is very fine (due to the relatively high cooling rates associated with the laser processing). Reference to the continuous cooling transformation diagram for 1085 steel (Ref. 23) indicates that an as-quenched hardness of 700 Vickers is typical for a martensitic/bainitic microstructure that would form under these cooling rates. Thus, the high hardness associated with the final pass can be attributed to the formation of as-quenched martensite, while the lower hardness values exhibited by the remaining section of the 1085 region can be attributed to tempering from the thermal treatment of subsequent layers. The hardness spike associated with the last layer would not pose a problem since it can be easily removed by machining prior to use. More importantly, actual use of the transition joint would involve the use of an alloy steel with lower carbon where this high hardness region may not form to begin with.

Future Directions

The results presented here demonstrate the feasibility of using the LENS process for fabricating graded transition joints for joining dissimilar materials. It is recognized that these results represent only a first step toward final resolution of the problem, and future research is required to optimize the transition joints for eventual reduction/elimination of DMW failures. In view of the DMW failure mechanism, a high-carbon steel would obviously not be used as part of the graded region. As previously noted, the high-carbon 1085 steel was used here for feasibility purposes only. The optimized gradient in carbon concentration across the graded region will likely have to vary from that typical of alloy steel (~ 0.10–0.15 wt-% C) to that of the pertinent stainless steel of interest, and more work is needed to identify the optimal gradient in both carbon and other alloying elements. However, the ability of the LENS process to fabricate graded transitions is independent of the powder composition, so this should pose no problem.

The formation of solidification cracks in the fully austenitic region of the grade also needs to be avoided, which should be easily accomplished by adjusting the composition in this range so that the solidification mode is FA instead of A or AF. Potential solidification mode shifts associated with the high cooling rates typical of laser processing will also need to be considered. The localized increase in hardness observed near the transition between the graded region and the 1085 side of the joint needs to be considered in more detail. This relatively high hardness is associated with the formation of high-carbon martensite and may not be a significant issue when lower carbon steel powders are used.

In addition, this region could be spread over larger distances by adjustments in the processing conditions, and subsequent heat treatment of the joint could be used to eliminate any remnant hardness spikes. Further work is required in this area. Any high hardness regions associated with the final layer are easily avoided by simply removing the last layer with a post-processing machining step. Lastly, more modern microstructural and mechanical modeling tools should be used to intelligently optimize the graded region based on factors such as microstructural evolution (during processing and in service) and corresponding compatibilities in thermal and mechanical properties.

Conclusions

A feasibility study was conducted to as-

sess the potential of the Laser Engineered Net Shaping process for fabricating graded transition joints between carbon steel and stainless steel alloys. The following conclusions can be drawn from this work:

1) A graded joint can be fabricated that exhibits a smooth transition in composition from 1085 steel to 316 stainless steel over a distance of ~ 2 in. Other grade lengths can also be prepared.

2) The transition joint consisted of four microstructurally distinct regions: an austenite region that existed over most of the grade, followed by a dual-phase austenite/martensite region near the interface between the grade and the 1085 steel, followed by a section of 1085 steel that appeared to be ferrite/bainite and tempered martensite, and then by the final layer with high hardness that appeared to be associated with the presence of as-quenched martensite.

3) Microstructural evolution within each of these areas can be understood by combining both nominal and localized composition measurements with the WRC and Schaeffler constitution diagrams.

Acknowledgments

The authors gratefully acknowledge the financial support of this work by the National Science Foundation through a PECASE Award, Grant No. DMI 9983968, made through the Division of Manufacturing and Industrial Innovation of NSF.

References

1. DuPont, J. N., and Marder, A. R., 1996. Dilution in single pass arc welds. *Metallurgical and Material Transactions B*, Vol. 27B, pp. 481–489.
2. Ornath, F., Soudry, J., Weiss, B. Z., and Minkoff, I. 1981. *Welding Journal* 60(7): 227-s.
3. Gittos, M. F., and Gooch, T. G. 1992. *Welding Journal* 71(12): 461-s.
4. Buchmayr, B., Cerjak, H., Kirkaldy, J. S., and Witmer, M. 1990. *Conf. Proc. Trends in Welding Science and Technology*, p. 237, ASM International, Materials Park, Ohio.
5. Klueh, R. L., and King, J. F. 1982. *Welding Journal* 61(9): 302-s.
6. Lundin, C. D. 1982. *Welding Journal* 61(2): 58-s.
7. Jones, W. C. 1974. *Welding Journal*, 53(5): 225-s.
8. Campbell, G. M., Elmer, J. W., and Gibbs, W. S. 1981. *Conf. Proc. Trends in Welding Research*, p. 443, ASM International, Metals Park, Ohio.
9. King, J. F., Sullivan, M. D., and Slaughter, G. M. 1977. *Welding Journal* 56(11): 354-s.
10. Ryder, R. H., Roberts, D. I., Viswanathan, R., and Prager, M. 1986. *Conf. Proc. Advances in Welding Science and Technol-*

ogy, p. 509.

11. Irving, B. 1992. *Welding Journal* 71(5): 27.

12. Smugeresky, J. E., Keicher, D. M. J., Romero, A., Griffith, M. L., and Harwell, L. D. 1997. *Advances in Powder Metallurgy and Particulate Materials*, parts 21–22, p. 33, Chicago, Ill., Metal Powder Industries Confederation, Princeton, N.J.

13. Griffith, M. L., Keicher, D. M., Atwood, C. L., Romero, J. A., Smugeresky, J. E., Harwell, L. D., and Greene, D. L. 2001. *Solid Freeform Fabrication Proceedings*, Austin, Tex., p. 125, University of Texas at Austin.

14. Liu, W., and DuPont, J. N. 2003. Fabrication of functionally graded TiC/Ti composites by laser engineered net shaping. *Scripta Materialia* 48: 1337–1342.

15. Liu, W., and DuPont, J. N. 2004. Fabrication of carbide reinforced titanium aluminide matrix composites by laser engineered net shaping. *Metallurgical and Materials Transactions*, Vol. 35A, pp. 1133–1140.

16. Noecker, F. F., and DuPont, J. N. Microstructural development and solidification cracking susceptibility of Cu deposits on steel, part I: direct deposition of Cu onto steel, accepted for publication in *Journal of Materials Science & Engineering*.

17. Griffith, M. L., Harwell, L. D., Romero, J. A., Schlinger, E., Atwood, C. L., and Smugeresky, J. E. 1998. *Solid Freeform Fabrication Proceedings*, Austin, Tex., p. 387, University of Texas at Austin.

18. Katayama, S., and Matsunawa, A. 1984. *Proc. ICALCO*, p. 60.

19. DuPont, J. N. 1999. Microstructural development and solidification cracking susceptibility in the fusion zone of a stabilized stainless steel. *Welding Journal* 78(7): 253-s to 263-s

20. Banovic, S. W., DuPont, J. N., and Marder, A. R. 2003. Dilution and microsegregation in dissimilar metal welds between super austenitic stainless steels and Ni base alloys. *Science & Technology of Welding and Joining* 6(6): 374–383.

21. Grange, R. A. and Stewart, H. M. 1946. *Trans. AIME*, Vol. 167, pp. 467–90.

22. Clyne, T. W., and Kurz, W. 1981. *Metall. Trans.*, 12A, p. 965

23. Atkins, M. 1997. *Atlas of CCT Diagrams for Engineering Steels*, p. 21, ASM International, Materials Park, Ohio.